

## THE 2011 JUNE 23 STELLAR OCCULTATION BY PLUTO: AIRBORNE AND GROUND OBSERVATIONS

M. J. PERSON<sup>1</sup>, E. W. DUNHAM<sup>2</sup>, A. S. BOSH<sup>1</sup>, S. E. LEVINE<sup>1,2</sup>, A. A. S. GULBIS<sup>1,3</sup>, A. M. ZANGARI<sup>1</sup>, C. A. ZULUAGA<sup>1</sup>, J. M. PASACHOFF<sup>4</sup>, B. A. BABCOCK<sup>4</sup>, S. PANDEY<sup>4</sup>, D. AMRHEIN<sup>4,5</sup>, S. SALLUM<sup>1,6</sup>, D. J. THOLEN<sup>7</sup>, P. COLLINS<sup>2</sup>, T. BIDA<sup>2</sup>, B. TAYLOR<sup>8</sup>, L. BRIGHT<sup>2</sup>, J. WOLF<sup>9,10</sup>, A. MEYER<sup>10</sup>, E. PFUELLER<sup>9,10</sup>, M. WIEDEMANN<sup>9,10</sup>, H.-P. ROESER<sup>9</sup>, R. LUCAS<sup>4</sup>, M. KAKKALA<sup>11</sup>, J. CIOTTI<sup>12</sup>, S. PLUNKETT<sup>12</sup>, N. HIRAOKA<sup>12</sup>, W. BEST<sup>6</sup>, E. J. PILGER<sup>13</sup>, M. MICHELI<sup>7</sup>, A. SPRINGMANN<sup>1</sup>, M. HICKS<sup>14</sup>, B. THACKERAY<sup>15</sup>, J. P. EMERY<sup>16</sup>, T. TILLEMANN<sup>17</sup>, H. HARRIS<sup>17</sup>, S. SHEPPARD<sup>18</sup>, S. RAPOPORT<sup>19</sup>, I. RITCHIE<sup>20</sup>, M. PEARSON<sup>20</sup>, A. MATTINGLY<sup>21</sup>, J. BRIMACOMBE<sup>22</sup>, D. GAULT<sup>23</sup>, R. JONES<sup>24</sup>, R. NOLTHENIUS<sup>25</sup>, J. BROUGHTON<sup>26</sup>, AND T. BARRY<sup>27</sup>

<sup>1</sup> Department of Earth, Atmospheric, and Planetary Sciences, Massachusetts Institute of Technology (MIT),

Cambridge, MA 02139-4307, USA; [mjperson@mit.edu](mailto:mjperson@mit.edu)

<sup>2</sup> Lowell Observatory, Flagstaff, AZ, USA

<sup>3</sup> South African Astronomical Observatory, Cape Town, South Africa

<sup>4</sup> Williams College-Hopkins Observatory, Williamstown, MA, USA

<sup>5</sup> Wesleyan University, Middletown, CT, USA

<sup>6</sup> Steward Observatory, University of Arizona, Tucson, AZ, USA

<sup>7</sup> Institute for Astronomy, University of Hawaii, Manoa, HI, USA

<sup>8</sup> Boston University, Boston, MA, USA

<sup>9</sup> Deutsches SOFIA Institut, Universitaet Stuttgart, Pfaffenwaldring 29, D-70569 Stuttgart, Germany

<sup>10</sup> SOFIA Science Center, NASA Ames Research Center, MS 211-1, Moffett Field, CA 94035, USA

<sup>11</sup> Leeward Community College, Pearl City, HI, USA

<sup>12</sup> Windward Community College, Kaneohe, HI, USA

<sup>13</sup> Hawaii Geophysics & Planetology, Honolulu, HI, USA

<sup>14</sup> Jet Propulsion Laboratory, California Institute of Technology, Pasadena, CA, USA

<sup>15</sup> Jet Propulsion Laboratory, Pasadena, CA, USA

<sup>16</sup> Department of Earth and Planetary Sciences, University of Tennessee, Knoxville, TN, USA

<sup>17</sup> United States Naval Observatory Flagstaff Station, Flagstaff, AZ, USA

<sup>18</sup> Carnegie Institute of Washington, Washington, DC, USA

<sup>19</sup> Research School of Astronomy and Astrophysics, Mt. Stromlo Observatory, Weston Creek, Australia

<sup>20</sup> EOS Space Systems, New South Wales, Australia

<sup>21</sup> IBM, St. Leonards, New South Wales, Australia

<sup>22</sup> James Cook University, Cairns, Queensland, Australia

<sup>23</sup> International Occultation Timing Association, Sydney, New South Wales, Australia

<sup>24</sup> Running Springs, CA, USA

<sup>25</sup> Cabrillo Observatory, Aptos, CA, USA

<sup>26</sup> Reedy Creek, Queensland, Australia

<sup>27</sup> University of Western Sydney, Penrith Observatory, Australia

Received 2013 January 31; accepted 2013 July 11; published 2013 August 29

## ABSTRACT

On 2011 June 23, stellar occultations by both Pluto (this work) and Charon (future analysis) were observed from numerous ground stations as well as the Stratospheric Observatory for Infrared Astronomy (SOFIA). This first airborne occultation observation since 1995 with the Kuiper Airborne Observatory resulted in the best occultation chords recorded for the event, in three visible wavelength bands. The data obtained from SOFIA are combined with chords obtained from the ground at the IRTF, the U.S. Naval Observatory Flagstaff Station, and Leeward Community College to give the detailed state of the Pluto–Charon system at the time of the event with a focus on Pluto’s atmosphere. The data show a return to the distinct upper and lower atmospheric regions with a knee or kink in the light curve separating them as was observed in 1988, rather than the smoothly transitioning bowl-shaped light curves of recent years. The upper atmosphere is analyzed by fitting a model to all of the light curves, resulting in a half-light radius of  $1288 \pm 1$  km. The lower atmosphere is analyzed using two different methods to provide results under the differing assumptions of particulate haze and a strong thermal gradient as causes for the lower atmospheric diminution of flux. These results are compared with those from past occultations to provide a picture of Pluto’s evolving atmosphere. Regardless of which lower atmospheric structure is assumed, results indicate that this part of the atmosphere evolves on short timescales with results changing the light curve structures between 1988 and 2006, and then reverting these changes in 2011 though at significantly higher pressures. Throughout these changes, the upper atmosphere remains remarkably stable in structure, again except for the overall pressure changes. No evidence of onset of atmospheric collapse predicted by frost migration models is seen, and the atmosphere appears to be remaining at a stable pressure level, suggesting it should persist at this full level through *New Horizon*’s flyby in 2015.

*Key words:* astrometry – Kuiper belt objects: individual (Pluto) – occultations – planets and satellites: atmospheres

## 1. INTRODUCTION

The higher capability of airborne observations compared with ground-based ones is highly beneficial for stellar occultation

observations; since the shadow path is often not over land, adverse weather frequently plagues ground-based observations whereas airborne telescope location can be optimized based on updated predictions until just hours prior to the event. Airborne

**Table 1**  
Event Parameters

Star Parameters	
Identifier	2UCAC24677089
Catalog position (J2000, at epoch of event)	$\alpha = 18\ 25\ 55.4890 \pm 0.1650$ arcsec $\delta = -18\ 48\ 07.047 \pm 0.064$ arcsec
Measured position (J2000, at epoch of event)	$\alpha = 18\ 25\ 55.4731 \pm 0.0075$ arcsec $\delta = -18\ 48\ 06.990 \pm 0.009$ arcsec
Pluto center ephemeris	
	JPL PLU017
Earth ephemeris	
	DE-405
Geocentric event parameters	
Midtime	UT 2011 06 23 11:24:11
Sky-plane velocity	23.81 km s <sup>-1</sup>

observations of stellar occultations have a long, successful history. NASA’s G. P. Kuiper Airborne Observatory (KAO), a modified C-141A jet hosting a 0.91 m telescope, began research operations in 1974. Some of the most notable results stemming from the KAO were the direct result of stellar occultation observations. These highlights include a central flash observation allowing characterization of the structure and extinction in the Martian upper atmosphere (Elliot et al. 1977b), the discovery of the Uranian ring system (Elliot et al. 1977a), the discovery of an atmosphere around Pluto (Elliot et al. 1989), and a measurement of the thermal structure of Triton’s atmosphere (Olkin et al. 1997).

The KAO was retired in 1995 and was succeeded by the Stratospheric Observatory for Infrared Astronomy (SOFIA). SOFIA is a modified Boeing 747SP with a 2.5 m telescope. SOFIA’s early science observations began in late 2010. Based on the success of stellar occultation observations with the KAO, one of the first-generation SOFIA instruments is the High Speed Imaging Photometer for Occultations (HIPO; Dunham et al. 2004). We present here results from the first attempt at observing a stellar occultation from SOFIA, that of the UT 2011 June 23 occultation by Pluto and Charon. The SOFIA observations were supported by extensive ground-based astrometry and a ground-based observing campaign at a total of 11 sites.

Pluto has been particularly well-studied via the stellar occultation technique. The first definitive detection of its atmosphere from the KAO revealed unexpected structure: the upper part of the light curve followed an isothermal profile, while just below the half-light level there was a “kink” below which the flux dropped more steeply (Elliot et al. 1989). This structure has been alternatively explained with models including atmospheric extinction (Elliot & Young 1992) and/or a steep temperature gradient (Hubbard et al. 1990). Multi-wavelength observations of a stellar occultation by Pluto were made in 2002 using SpeX on the Infrared Telescope Facility, the results of which demonstrated that some extinction was present at that time (Elliot et al. 2003a; Pasachoff et al. 2005) due to the changing extinction between near- and far-infrared observation bins. In addition, Pluto’s atmospheric pressure at a constant radius had increased by approximately a factor of two since 1988 (Elliot et al. 2003a; Sicardy et al. 2003; Pasachoff et al. 2005). Such a significant change could be at least partly explained by frost migration models (Hansen & Paige 1996), with the largest change expected near perihelion (in 1989). The next stellar occultation by Pluto was observed in 2006 (Young et al. 2008; Elliot et al. 2007), demonstrating that the atmosphere had changed only slightly between 2002 and 2006 and that atmospheric extinction had dissipated.

In 2007, observations of a grazing occultation revealed waves in Pluto’s upper atmosphere (McCarthy et al. 2008; Person et al. 2008). These have been attributed to internal gravity waves, possibly with some contribution from Rossby waves (Hubbard et al. 2009; Person et al. 2008).

The results from the various occultations have been compared to computational ice/frost migration models on Pluto’s surface, in an attempt to constrain various parameters of Pluto’s surface (Hansen & Paige 1996). As Pluto moves through its orbit, different areas of the surface are illuminated, forcing nitrogen ice to sublime in the sunlit areas, supporting the atmosphere, and recondensing in the darker areas. As Pluto came through its equatorial plane crossing in the early 1990s, the entire surface was illuminated before the south pole receded from view. This global illumination, providing no cold refuge for frost traps, is the mostly like cause of the great increase in atmospheric pressure seen between the KAO event and the ground-based occultations. As the southern pole moves deeper into shadow, models predict that the atmosphere should begin a significant collapse, although the details of this collapse and its timing are open to interpretation depending upon what models are selected (Young et al. 2011).

## 2. ASTROMETRY AND PREDICTION

### 2.1. Identification and Selection

The selection of the UT 2011 June 23 occultation occurred late in 2010, and was based on six years of astrometric data for Pluto and updated star position data that showed the predicted path to be in a suitable location for SOFIA access. We applied for HIPO time on SOFIA in conjunction with previously planned SOFIA test and characterization work. Event parameters are listed in Table 1. This was a good event for SOFIA because Pluto was visible within SOFIA’s elevation angle range, the ground track allowed us to deploy from its normal base in Palmdale, CA, the event occurred at a time of year that was compatible with HIPO’s testing schedule, and the shadow path would remain accessible to SOFIA even if updated astrometry led to moderate shifts. From an astrometric viewpoint, the occultation star was known to be relatively isolated, the event occurred late enough in the Pluto observing season to allow us to refine the prediction with earlier astrometry; there was another Pluto event only six weeks earlier that confirmed the accuracy of our predictions (Sallum 2012), and the event occurred early in the morning thus allowing a full night of astrometry on the event night in order to send path updates to the SOFIA flight team.

**Table 2**  
Telescopes Used to Collect Astrometric Data on Pluto Field, 2011 March–June

Telescope	Diameter (m)	Focal Length (m)	Instrument(s)	Pixel Scale (arcsec pixel <sup>-1</sup> )	FOV (arcmin)
U.S. Naval Observatory Flagstaff Station, Flagstaff, AZ (USNO-FS)					
Kaj Strand	1.55	15.2	1 chip	0.183	6.5 × 12.5
			Tek2k	0.325	11 × 11
Lowell Observatory, Flagstaff, AZ					
Astrograph (Mars Hill)	0.5	4.0	Snapshot CCD	0.845	29 × 420 <sup>a</sup>
Hall telescope (Anderson Mesa)	1.07	8.4	NASA42	0.369	25 × 25
Cerro Tololo, Chile					
Small and Moderate Aperture Research Telescope System (SMARTS)	0.9	12.15	cfccd	0.396	14 × 14

**Note.** <sup>a</sup> The CCD on the astrograph uses time–delay–integration and therefore can take “strips” of any length. This is the length of the Pluto strips for 2011.

**Table 3**  
Astrometric Data Collected for Prediction Refinement (2011 June)

Telescope/Instrument/UT date	Number of Frames	Average Seeing (″)	Standard Deviation of Star Data (R.A./decl.) (″)	Standard Deviation of Pluto Data (R.A./decl.) (″)
L42/NASA42/0611	15	2.0	0.013/0.023	0.016/0.029
L42/NASA42/0612	20	2.5	0.015/0.035	0.017/0.029
L42/NASA42/0613	10	1.5	0.007/0.020	0.013/0.010
USNO61/1CHIP/0618	3	1.7–2.2	0.007/0.006	0.019/0.006
USNO61/1CHIP/0619	14	2.0–2.7	0.004/0.010	0.006/0.013
USNO61/1CHIP/0620	4	2.0–3.0	0.002/0.006	0.012/0.010
USNO61/1CHIP/0621	30	1.7–1.9	0.014/0.015	0.022/0.018
USNO61/1CHIP/0622	24	1–1.5	0.013/0.009	0.006/0.009
USNO61/1CHIP/0623early	48	1.8–2.0	0.013/0.012	0.016/0.012
USNO61/1CHIP/0623late	16	1.0–1.2	0.013/0.008	0.006/0.008

## 2.2. Early Refinement

Once Pluto became available in the morning sky during the spring of 2011, we acquired astrometric measurements to refine our ephemeris correction model (ECM) for Pluto (A. S. Bosh et al. 2013, in preparation), using data from the telescopes listed in Table 2.

## 2.3. Astrometric Accuracy and Duplicity Search

For this event, our goal was to place SOFIA within Pluto’s central flash zone. There had been only one previous clear observation of Pluto’s central flash (Olkin et al. 2007), at  $\sim 75$  km from the shadow center. Our goal was to produce a prediction accurate to  $\pm 50$  km or  $\pm 0''.0025$ .

The accuracy of Pluto astrometry in the few days before an event depends on the accuracy of (1) the astrometric reference network, (2) centroiding, and (3) Charon’s ephemeris, as well as systematic errors if the star to be occulted is double or multiple. We use UCAC2 (Zacharias et al. 2004) for our reference network. Beyond any zonal issues present, in general the accuracy of the catalog ( $\sim 35$  mas) at the current epoch has decreased due to proper motion errors being propagated forward  $\sim 15$  yr.

Perhaps the largest potential effect to consider in our astrometry is the possibility that the target star may be part of a multiple system. With more than 60% of stars estimated to be double or otherwise multiple, this is a possibility that must be explored. As an example, an unresolved companion star with a separation of 0.25 arcsec and  $\Delta m = 1.0$  would offset the measured center by 0.1 arcsec and thus dwarf all other effects. To check

for duplicity, we investigated data taken at the Magellan Observatory, with a pixel scale of 0.188 arcsec pixel<sup>-1</sup> and seeing of  $\sim 0.66$  arcsec. Using the ISIS package (Alard 2000), Georgi Mandushev (Lowell Observatory) created a model of the point-spread function (PSF) as a function of position in the field and subtracted the fitted PSF at the position of the target star. No other stars were visible in the subtracted image, to a limit of  $\Delta m \sim 4$  mag.

As an additional check for companions of this star, Adam Kraus (IfA) was able to acquire images using *J*-band adaptive optics imaging (natural guide star) on Keck, just a few hours before the occultation. These images showed no companion within 0.04 arcsec for  $\Delta m = 0$ .

While these types of measurements cannot rule out the possibility of a systematic shadow shift due to multiplicity of the occultation star, we at least reduce the chances of an unexpected surprise by narrowing the parameter space in which a companion star can be hiding. In this case, we remain unable to rule out a  $< 20$  mas shift in shadow position due to this effect.

## 2.4. Final Refinement/In-air Course Correction

In the 12 days before the event, Pluto and the occultation star were in the same field of view (FOV) as observed with the Lowell 42 inch telescope and then the USNO 61 inch telescope. During this time, we obtained three nights of data on the Lowell telescope, followed by six nights of data on the USNO-FS telescope (Table 3). Because there is a common FOV for these data, we can ignore small field-to-field differences in the astrometric reference network. The remaining effects include

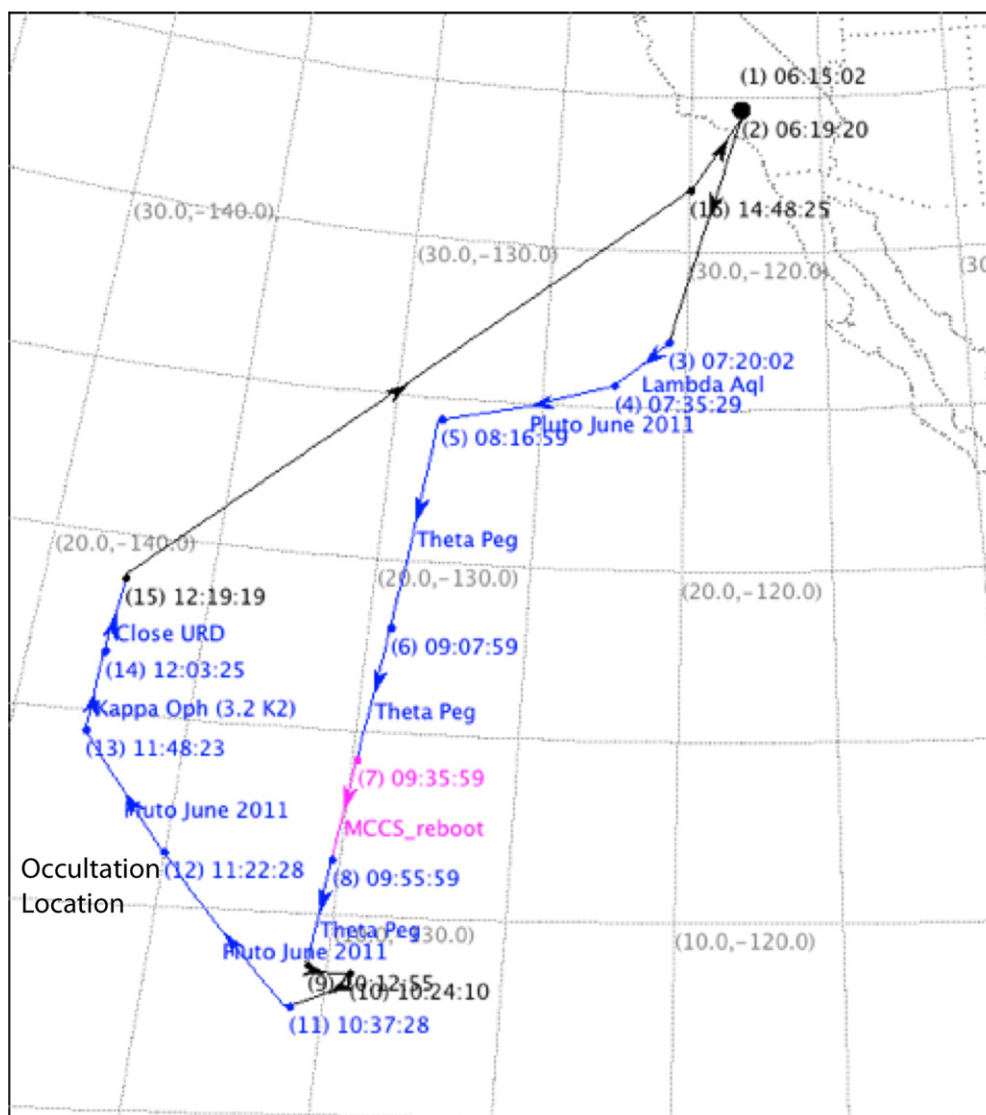


**Figure 1.** Flight plan for the SOFIA occultation flight. Latitude and longitude are noted in degrees, each leg of the flight is numbered and labeled as to observational target, and the occultation location is marked with a blue dot on the occultation leg.

unmodeled field distortions and the effect on the solution of a small number of “rogue” reference stars in the network. These are assumed to be stars whose positions at epoch of date may be inaccurate due to the extrapolated effect of proper motions. Beginning on June 20, we provided daily astrometry updates to the SOFIA flight planners to use in designing flight plans for the test flight and the occultation flight.

On the night of the event, data collection began at USNO-FS as soon as it was dark in Flagstaff. These data were transferred to MIT and analyzed within minutes. Unfortunately, the seeing at the beginning of the evening was very poor,  $\sim 2$  arcsec; later in the evening, Pluto was blended with a field star near the occultation star. Several hours into the occultation flight, the observing team aboard SOFIA called the astrometry team at MIT using a satellite telephone to get what was expected to be the final update: fly 323 km north of the reference solution. This change was conveyed to the FAA, which rejected the proposed course correction. The flight team decided to wait a short time before trying to get FAA approval again.

Shortly after this update was communicated, the Flagstaff seeing improved to 1–1.5 arcsec. Pluto also separated from the

field star and was temporarily isolated before heading for the occultation star. Observations continued at USNO-FS, data were transferred and analyzed, and it became clear that these latest data suggested a small difference in offset. One hour after the “final” call from SOFIA, at 2.5 hr before event midtime, the SOFIA team called the MIT astrometry team again. This time, a different offset was given: fly 232 km north of the reference solution. This new proposed course correction was sent to the FAA, which approved it. SOFIA turned to the occultation leg of the night’s flight. Due to the last-minute course corrections, SOFIA’s final path was a few seconds late and a small amount north of the final update. The flight path is shown in Figure 1.

### 2.5. Discussion of Prediction Results

The astrometric measurements yield offsets of Pluto from its ephemeris and of the target star from its catalog position (Table 1). The measured star position in Table 1 was determined using 24 frames of USNO61/1CHIP data and provides a measure of the overall star error remaining on the day before the event. We model Pluto’s ephemeris offset with our

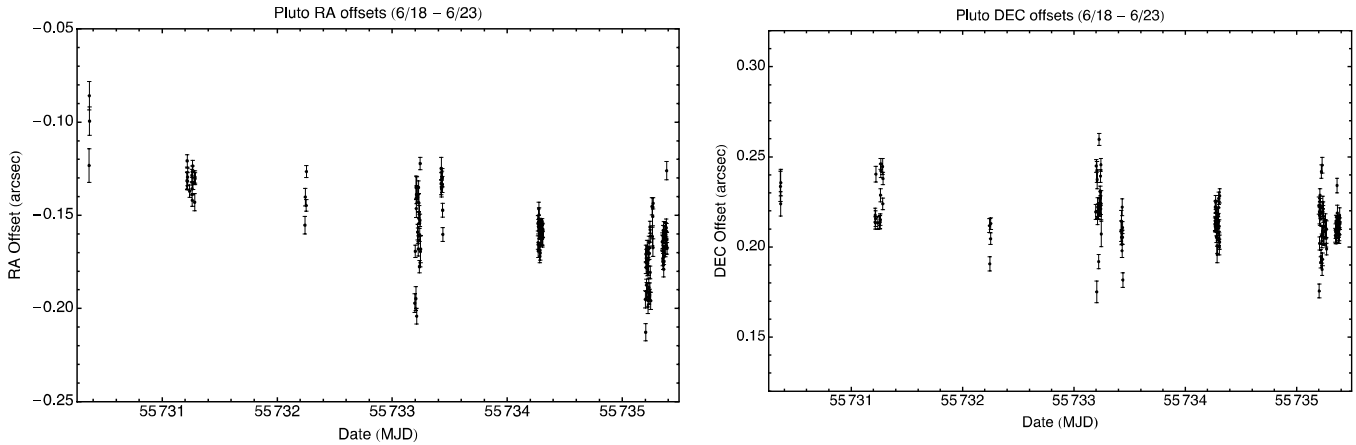


**Figure 2.** Offsets of Pluto from its ephemeris, plotted vs. time during the last week of astrometry before the occultation.

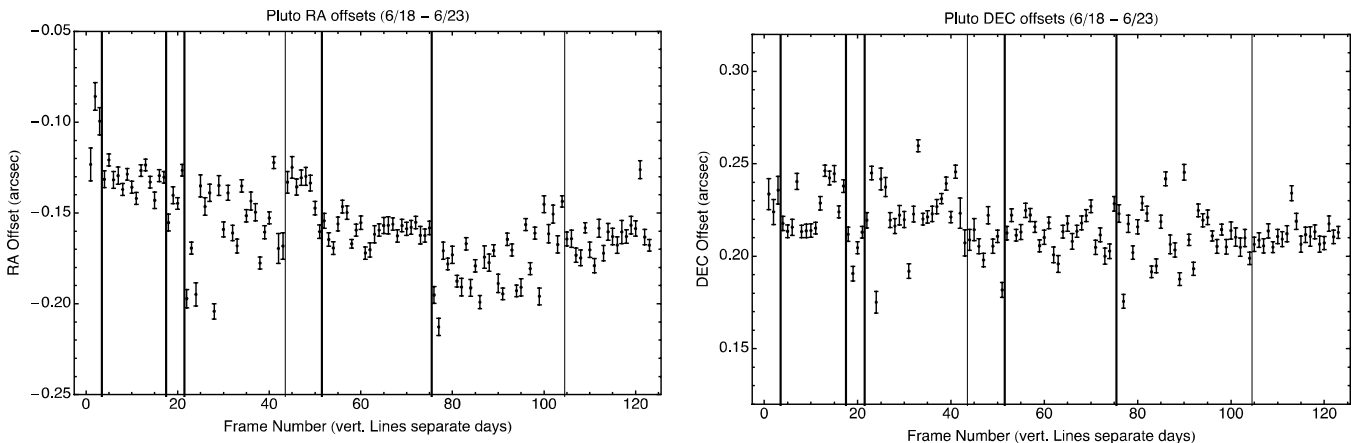


**Figure 3.** Offsets of Pluto from its ephemeris, plotted vs. frame number during the last week of astrometry before the occultation. The thick vertical lines indicate night boundaries, and the thin vertical lines indicate a short gap in observations during a night.

time-dependent ECM (A. S. Bosh et al. 2013, in preparation), but for the final astrometric update, we switched to a constant offset model. In theory, any inaccuracies in Charon’s orbit would show up in our offsets so we should have a sinusoidal offset with Charon’s period, but in practice, during the time period of these data, the seeing was too poor, which led to large standard deviations in our data, and we determined that we would not be able to model any putative offset due to Charon. In Table 3, we present a summary of the data taken during this prediction refinement effort. Note the varying data quality during the week; while we were very lucky to have clear weather for the week preceding this event, the nights were not uniformly good. In fact, under normal circumstances, we would have declared several of the nights to be too poor for astrometry due to the large seeing disks, which are particularly problematic in the very crowded Pluto field.

In Figures 2 and 3, we present the measured offsets for Pluto on the six nights during and before the occultation. Figure 2 shows the offsets versus time, while Figure 3 shows the same offsets versus frame number. In these figures all points represent data taken with the same detector on the same telescope and we notice several features. One feature is that the scatter of the data points is not uniform; we see the periods of poor seeing fairly easily here as periods of greater than normal scatter. Another feature to notice is that the overall declination offset appears to be constant. The  $\delta$  offset maps mainly as a north–south offset of the event shadow on the Earth, and therefore is most directly the

quantity that we want to determine in order to calculate where to send SOFIA. A third feature of these plots is that the right ascension offset may not be constant. The  $\alpha$  offset maps mainly as an offset in the event time, so the exact value of this offset is less critical. There are two possible causes for the variable  $\alpha$  offset. On the nights of UT June 21 and 23, Pluto was blended with a field star for part of each night; in both cases the field star was separated from Pluto mainly in the  $\alpha$  direction. Thus, Pluto centroiding could have been affected. If we disregard data from June 21 and the early part of June 23, then we see a small but significant slope to the  $\alpha$  offset versus time:  $0.013 \pm 0.004$  arcsec day $^{-1}$ . This is likely due to Pluto’s ECM, which we did not use for the final prediction.

While the daily astrometric updates were based on data from the entire week, for the in-flight updates on the night of the event, we instead used data only from the occultation night. In Figure 4, we show three offsets: (1) in black, the early-evening offset, which was conveyed to the flight crew during the first (and only planned) telephone call, (2) in blue, the mid-evening offset from a smaller subset of frames taken when Pluto was isolated and the seeing had improved dramatically; this offset was conveyed to the flight crew during a second telephone call, and (3) in green, the actual Pluto offset as derived from our central flash observation and assuming that our measured star position is correct. The final impact parameter for SOFIA (see later sections for generation of the geometric solution) was calculated to be  $104 \pm 3$  km or  $0.0046 \pm 0.0001$  arcsec.

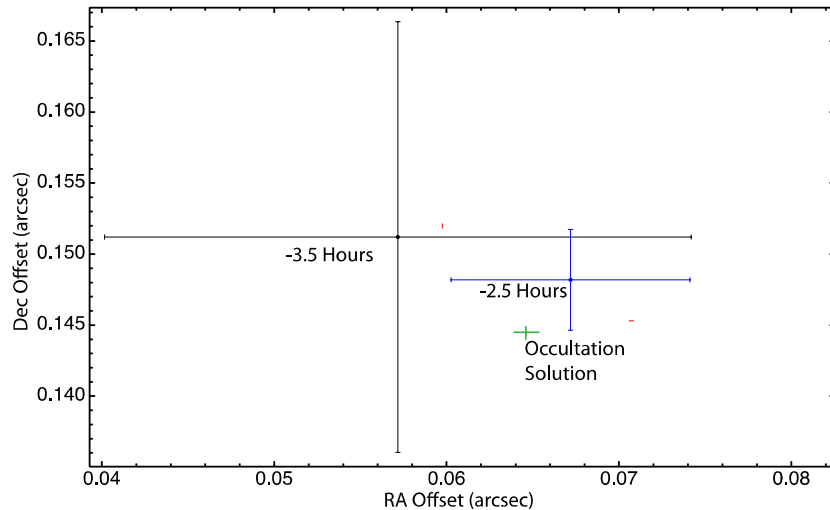


**Figure 4.** Pluto astrometry from USNO-FS with 1 chip on UT 2011 June 23. The black position update was sent to the flight crew at 3.5 hr before the event, the blue position update was sent at event  $-2.5$  hr. The green solution is that produced by the occultation geometric solution assuming the final star position was accurate. (The green error bars are inflated by a factor of three for visibility, as the geometric solution provides essentially a single location at this scale.)

### 3. DATA AND LIGHT CURVES

#### 3.1. SOFIA

Individual light curves were generated for each of the three CCDs that were used to observe the occultation on SOFIA: HIPO blue channel (sampled at 1 Hz), HIPO red channel (2 Hz), and the Fast Diagnostic Camera (FDC; 4 Hz). Before light-curve creation, HIPO images were overscan-corrected and then flattened using lab-created flats. FDC images were bias-corrected. Using IRAF (Tody 1986), synthetic aperture photometry was used to create each light curve. For the two HIPO channels, light from an aperture containing Pluto, Charon, and the occultation star was compared against the summed flux of 11 bright stars on the frame. The signal-to-noise ratio (S/N) of the pre-event baseline was calculated for a variety of apertures: a circular aperture radius of 4.5 pixels or  $4''.5$  at roughly  $1''$  per  $3 \times 3$  binned pixel (Dunham et al. 2008) was chosen as the greatest S/N for both channels. The same procedure was repeated for the FDC, though the smaller field of view allowed for only three comparison stars. The optimum aperture was found to be 4.0 pixels ( $\sim 2''.2$ ) in radius.

Symmetric sections of the pre- and post-event baselines were used to normalize the upper baselines to 1, representing the combined flux of Pluto, Charon, and the occultation star. The curves were calibrated by examining images taken approximately three hours before the predicted occultation, when Pluto–Charon and the target star were well separated. This background fraction was subtracted from the data such that a zero-level flux represents Pluto and Charon alone. For HIPO blue, HIPO red, and the FDC, the individual background fractions were 0.670, 0.403, and  $0.532 (\pm 0.011)$ , respectively.

#### 3.2. IRTF

We were awarded a 5 hr observing window, centered on the predicted midtime, at NASA’s 3 m Infrared Telescope Facility (IRTF) on Mauna Kea, HI. Data were taken with MORIS (the MIT Optical Rapid Imaging System; Gulbis et al. 2011) and SpeX (Rayner et al. 2003). The SpeX  $0.9 \mu\text{m}$  dichroic was used to direct the visible-wavelength portion of the beam into MORIS. The plate scale of MORIS is  $0.114 \text{ arcsec pixel}^{-1}$ , for a  $60 \text{ arcsec}^2$  field of view. No filter was used for MORIS, which

ran in full frame, conventional mode with a gain of  $2.4x$  and was cooled to  $-65^\circ\text{C}$ . Low-resolution spectra were taken with SpeX over the range of  $0.9\text{--}2.5 \mu\text{m}$ , which will be analyzed elsewhere (A. A. S. Gulbis 2013, in preparation).

The MORIS occultation data consisted of an 18,000 frame datacube having a cycle time 0.3 s, of which 1.7 ms was deadtime. Each frame was triggered by the GPS starting at 10:45:00 UT. Calibration images were taken with the occulted star and Pluto well-separated from each other.

Aperture photometry was performed using Mathematica (Wolfram 1991) on each frame of the MORIS occultation data to extract the combined Pluto–Charon plus occultation star signal as well as two comparison stars. The data were bias-subtracted and flat-fielded. A square aperture of 35 pixels per side was used for the comparison stars. A variable aperture size was used for the combined Pluto–Charon plus star signal: the aperture decreased from 45 to 35 pixels as Pluto and Charon moved closer to the star. The light curve was calibrated and normalized as for the SOFIA light curves. The background fraction was  $0.51 \pm 0.02$  for both MORIS and Spex.

#### 3.3. USNO-FS

The occultation was observed with a six-chip e2v array on the US Naval Observatory, Flagstaff Station’s 1.3 m telescope. The pixel scale is 0.6 arcsec for this detector, for a field size of approximately  $20 \times 40 \text{ arcmin}$ . The camera controller was GPS synchronized for absolute timing measurements. Image subframes were read to reduce the overhead between successive exposures to 2.253 s. Exposure times were 5 s, for an overall observing efficiency of 67%. All images were taken through an SDSS  $i'$  filter. As can be seen in the light curve, the usable data end just after Pluto’s emersion due to the rising Sun.

The occultation images were bias-subtracted and flat-field-corrected using standard tools in IRAF. On each image, we identified 12 stars. Centroids for each were computed using marginal analysis. Eight of these stars were measured to compute a mean estimate of the seeing in each image. We used an aperture with a radius of 0.75 FWHM for all the relative aperture photometry. This was not the highest signal-to-noise aperture, but provided a good compromise for the later images when the sky background was increasing due to impending sunrise, and very low field altitude.

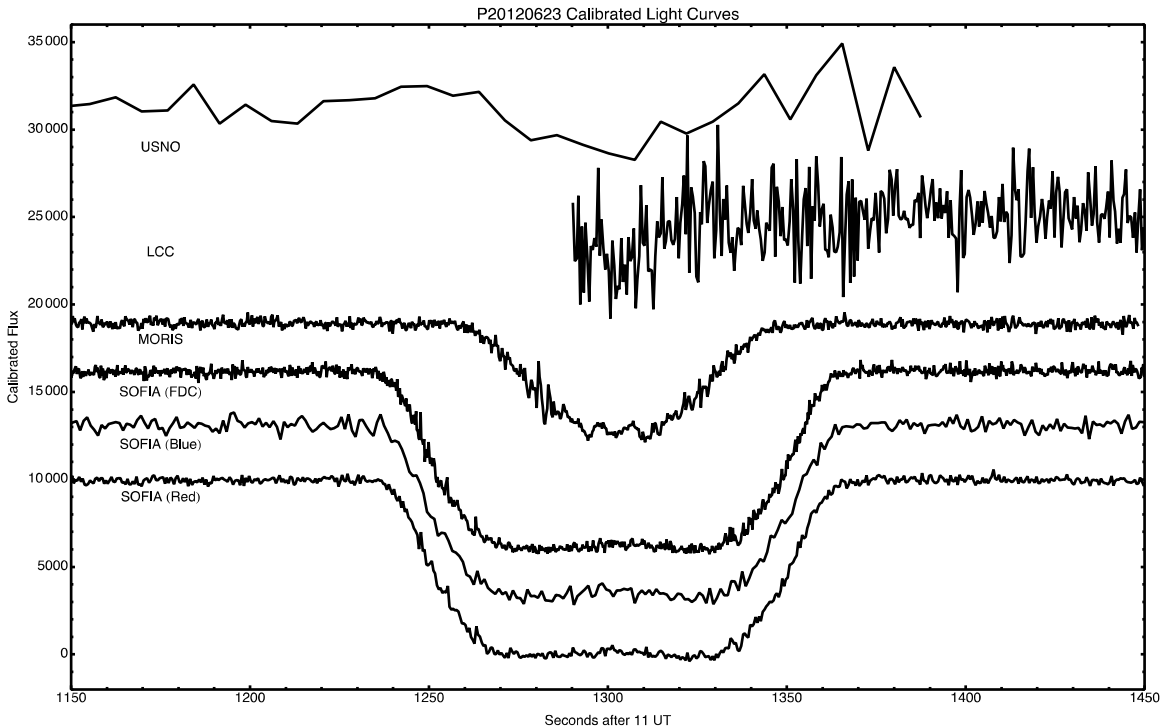


**Figure 5.** All Pluto light curves obtained. Plotted above are all light curves obtained in this effort, each normalized from 0 to 10,000 counts. Light curves are ordered from north to south and offset from each other by 3000 counts for clarity of comparison; the LLC and USNO-FS light curves are offset by 6000 counts due to their higher noise). Note that all three of the SOFIA light curves show a wide but shallow central bulge slightly offset to the right. See also the change in slope between the upper and lower portions of the SOFIA light curves. This occurs at about the same location as that seen in the 1988 Pluto light curve (Millis et al. 1993) but changes in the opposite direction becoming suddenly shallower rather than steeper with increasing atmospheric depth.

Mean sky values were computed in an annulus around each object with an inner radius of 5 FWHM, and an outer radius of 10 FWHM. Point sources falling within the annulus were excluded. For comparison objects, we used two stars that were of comparable brightness and showed no obvious variability over the period of the event.

The final relative light curve was computed as the ratio of the flux from the occultation star plus Pluto and Charon with respect to a single comparison star with a second comparison star used as a check.

### 3.4. Leeward and Windward Colleges

Weather at Windward Community College (HI) prevented observations. Data from Leeward Community College (HI) were obtained using the 0.5 m Ritchey–Chretien telescope, with an SBIG ST-9 imager and no filter. Images were taken at an integration time of approximately 0.25 s with a full cycle time of 0.5 s. The images have a plate scale of 0.44 arcsec pixel<sup>-1</sup>.

Due to time constraints, no calibration images were taken, and so raw data frames were reduced using three comparison stars. Technical issues and weather caused the observations to be started while the occultation was in progress, so data was only acquired from the area just before the occultation mid-time through emersion. Reduction was done with varying size apertures, with the highest signal-to-noise ratio coming from a 2.64 arcsec (6 pixel) aperture box. The resulting light curve was normalized according to the procedure used for the IRTF/MORIS data discussed above.

### 3.5. Final Light Curves

Figure 5 shows a plot of all light curves obtained and used in this analysis. Note that the Leeward and USNO-FS light curves,

while consistent with the MORIS and SOFIA curves, have a much lower S/N, as well as incomplete coverage of the event. When included in subsequent fitting, S/N weighting serves to give them very little leverage over the fitted parameters, but their location and depths still provide checks against the fitted model as determined by the higher quality curves.

The three SOFIA curves bottom out at the calibrated zero flux level (within photometric error bars), while the MORIS, LCC, and USNO-FS curves do not reach that deep, representing grazes in the upper atmosphere.

## 4. ANALYSIS

### 4.1. Geometric Solution

The light curves generated from the successful observing stations were simultaneously fit to an analytic atmospheric model to generate a preliminary solution to both the geometric location of Pluto with respect to the occultation star, and the radius of Pluto’s atmosphere at the half-light level. The model used was a modified version of the Elliot & Young model (1992) adjusted to use distance and direction from Pluto as the base independent variable rather than time before or after the occultation.

These distances were calculated by coupling the locations of the observing telescopes (carefully noting the changing GPS coordinates of SOFIA during the event) and combining these with Pluto’s ephemeris, using the standard rotation of Pluto’s JPL XYZ-ephemeris into the FG-plane (Elliot & Olkin 1996) around our measured position for the occultation star (Table 1). This leaves a small offset, ( $f_o$ ,  $g_o$ ), between the calculated and observed occultation centers on the sky plane that accounts for any linear offsets in Pluto’s actual ephemeris and the true occultation star position.

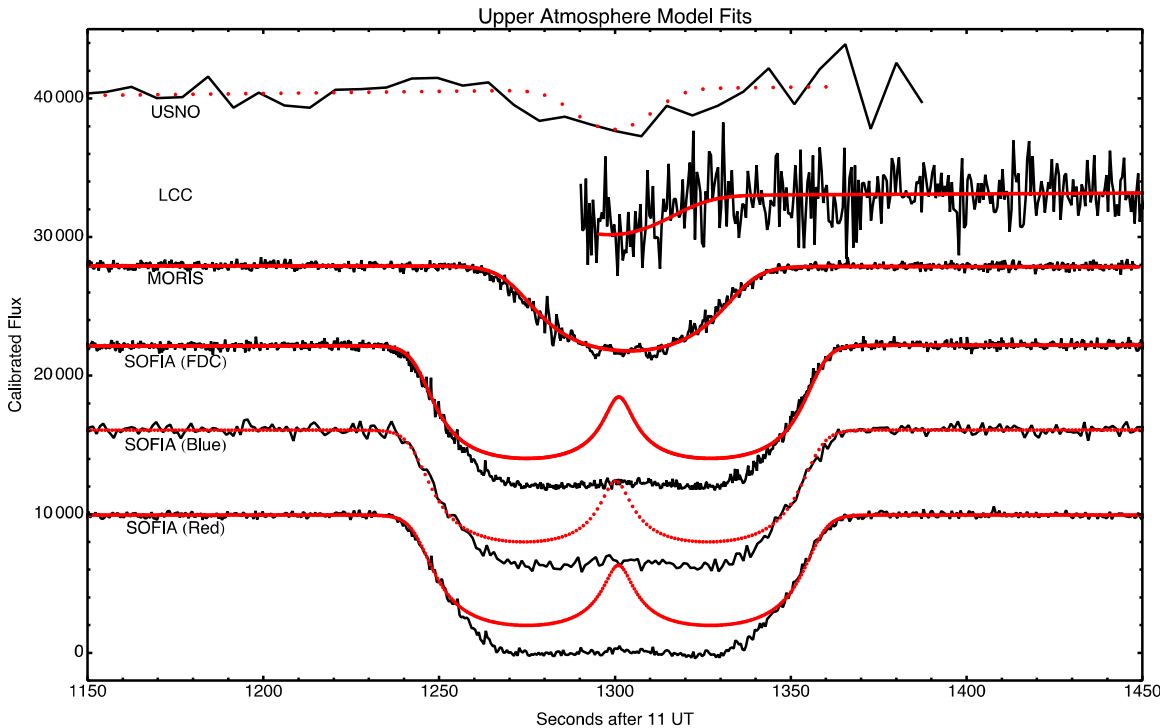


**Figure 6.** Upper atmospheric fits to the data. Similar to Figure 5, we plot all of the light curves normalized to 10,000, with each light curve offset by 6000 for clarity. Plotted in red is the best-fitting model for the data. Note that the models fit only the upper portion of the data. As depicted, based upon the upper atmosphere alone, we would expect very large central flash signatures for the three SOFIA light curves whereas only small central flashes are actually seen in the data.

Fitting all of the light curves simultaneously to the model, weighted according to their relative signal-to-noise ratios, resulted in this geometric Pluto center,  $(f_o, g_o) = (-3673.2, 4408.9)$  km  $\pm$  (0.9, 1.8). This center is used to determine the closest approach distance between each telescope and the center of Pluto’s shadow later in the analysis. All fits discussed in the coming sections were robust to this centroid parameter, with all fitted values agreeing to within  $2\sigma$  errors.

As has been performed on a previous Pluto–Charon occultation (Sicardy et al. 2009), using this fitted center and the fitted center for Charon derived from the contemporaneous occultation of the same star, the precise distance and direction between Pluto and Charon can be determined, greatly constraining the current Pluto–Charon ephemeris. These results will be presented in another publication (A. S. Bosh et al. 2013, in preparation).

#### 4.2. Pluto’s Upper Atmosphere

Beyond the geometric portion of the solutions, this simultaneous fit to all light curves also results in best-fit values for various atmospheric parameters. This fit is only applied to the upper atmospheric points in the light curves. As seen in Figure 5, the atmosphere behaves distinctly differently between the upper and lower sections of the light curve data. The station penetrating deepest into the atmosphere, SOFIA, has a change in slope around half-light reminiscent of (though to a lesser extent than) the “kink” or “knee” first seen in 1988 from the KAO (Millis et al. 1993). Indeed the best-fitting models for the upper portions of these light curves fail to fit the lower portions. For this analysis, we define the separation between the upper and lower portions of the light curve as occurring at half-light (0.5 normalized stellar flux) and only fit models to the data in the upper portions of the light curve. Figure 6 shows the best-fitting adopted model for the upper-half of the light curves.

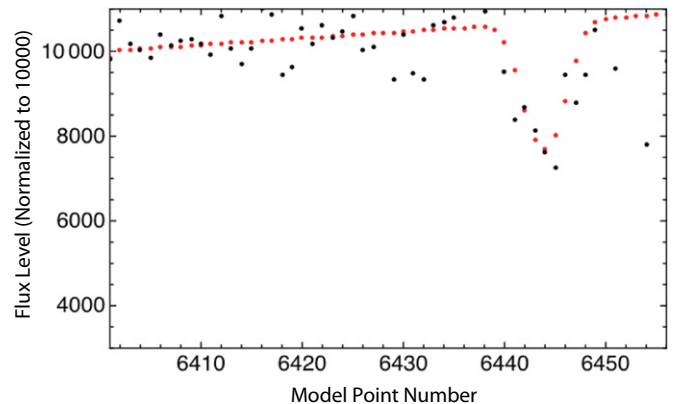


**Figure 7.** Plot of the best-fitting model over the USNO light curve. In this model, plotted in red, the USNO data (black points) were not fit. They are merely presented with the resulting model from fitting the other light curves as a check of the model reliability. Note that even the shallow depth (never less than 7000) of the light curve is accurately reproduced by the model. The final points of the light curve are perturbed by the rapidly changing sky brightness at sunrise.

While Figure 6 appears to be dominated by noise for the two northern-most light curves, the model matches their behavior. As a check, the noisy USNO light curve was left out of one fit, and then the resulting model was overplotted on the data. This result is given in Figure 7. The full data set, including the USNO and Leeward Community College light curves, were used in all subsequent atmospheric fits, although the low S/Ns of these two curves resulted in over an order of magnitude less weighting and thus little leverage over the fits.

The first fitted parameter of interest from the best fitting model is the occultation half-light radius (the radius in the atmosphere at which the occultation light curve drops to half its original flux due to refraction), which is here measured to be

**Table 4**  
Shadow Radius of Pluto Occultations (Constant Atmosphere)

Year	Shadow Radius (km)	Source
2006	1208 ± 4	Elliot et al. 2007
2007	1207 ± 4	Person et al. 2008
2010	1226 ± 12	Person et al. 2010
2011	1205 ± 2	This work

1288 km ± 1 km. The determination of this radius depends closely on the choice for atmospheric scale height and temperature profile fed to the model.

In this case, we used a common reference atmosphere, derived in previous work (Elliot et al. 2007; Person et al. 2008, 2010), of assuming a thermal binding parameter ( $\lambda$ ) of 18.3, and a temperature gradient parameter ( $b$ ) of  $-2.2$ . These parameters are fully described in Elliot & Young (1992). These, while not necessarily the correct parameters at the moment, allow the fitted half-light values of several different occultations to be directly compared. Table 4 gives the equivalent shadow radius values from the last several occultations measured using this method.

Table 4 shows that the shadow radius has remained constant over the last half decade, with the exception of one possible excursion during 2010. While the error bar of that point is much larger than that measured in the surrounding years, it is still low enough to indicate a possible singular change on a short timescale that has returned to the earlier value. It might also be due to variations over Pluto’s surface as all of the light curves from the 2010 occultation were samples on the northern-most limb of Pluto with very little global coverage constraining the solution (Person et al. 2010).

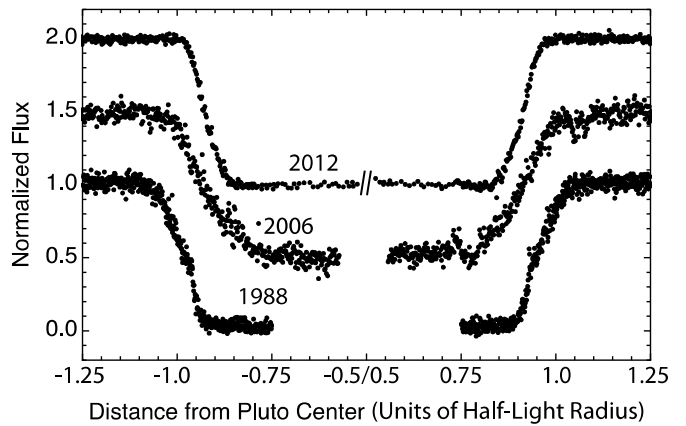
However, a more complete story appears if, rather than comparing shadow radii assuming a constant atmospheric profile, one allows the upper atmosphere to give its best fitting solution to the data in each event. These results are given in Table 5.

Table 5 shows that the pressure scale height of the atmosphere has remained remarkably constant over the past half decade, after changing considerably from the value measured in 2002. This scale height is accompanied by a commensurate stability in overall radius and temperature with slight fluctuations in these parameters counteracting each other to produce a consistent scale height. This feature even persists back to 1988, where the best fitting scale height to the full P8 occultation data set was  $56 \pm 5$  km, while the half-light radius was a low  $1233 \pm 4$  km, counteracted by a high half-light temperature of  $114 \pm 9$  K.

Throughout the significant changes we have seen on Pluto, the pressure scale height appears to have remained remarkably constant, with temperature and atmospheric radius changing in unison to compensate even the doubling of atmospheric pressure seen between 1988 and the current era.

#### 4.3. Pluto’s Lower Atmosphere

While the upper atmospheric scale height has remained constant with temperature and half-light radius somewhat less



**Figure 8.** Light curves vs. half-light radius distance. Light curves from 1988 (Millis et al. 1993), 2006 (Gulbis et al. 2006), and 2012 (this work) are plotted on the same radius scales to show overall evolution. The 2012 light curve is cut off at the half-light radius (center of the plot) and the scale is divided at 0.5 radii for ease of comparison, as neither of the older curves get any closer to the center than that. The nearly central 2012 chord penetrates much deeper into the atmosphere. Note that the 1988 and 2012 light curves have steeper, more linear sides than the 2006 light curve, which is more rounded. Both come out to a flat bottom, with a sharp angle in the descent, while the 2006 curve only gradually bottoms out and is more rounded.

so, the lower atmosphere has undergone significant changes. The first is seen in the structure of the lower light curves for nearly central chords. As described by Elliot et al. (2007), the early 1988 light curve had a clear slope change at half-light, but this feature was gradually washed out through later years with the light curve becoming progressively smoother (bowl-shaped) in 2002 and then 2006. (See Elliot et al. 2007, Figure 6.) However, as seen in Figure 8, the steep sides and slope change from the 1988 data appear to have returned, although the slope below half-light is bending inward rather than outward, as was seen in the 1988 curve.

Other than this gross comparison of light curves, characterizing this lower atmospheric evolution is not straightforward. There are two generally accepted possibilities for the changes in the lower portion of the atmospheric profile compared to the upper portions. These are discussed in the following two sections.

#### 4.4. Haze-model Fitting

This model was the first used to explain the shape of the 1988 light curve including the sudden onset “kink” (Millis et al. 1993). It essentially modifies the Elliot & Young (1992) model by adding three haze parameters, one for the upper onset altitude of the haze, one for the scale height of the haze, and the third for the altitude at which the haze achieves optical depth unity. Not intending to explain the precise nature of the haze, it merely allows the occultation starlight to suffer extinction based on the optical depth of the supposed haze at each altitude. Above the onset altitude, the atmosphere is assumed to be clear and the light is reduced only by normal refraction.

**Table 5**  
Half-light Radius of Pluto Occultations (Free Atmosphere)

Half-light Parameter	1988 June 9	2002 August 21	2006 June 12	2007 March 18	2011 June 23
Radius (km)	1233 ± 5	1279 ± 5	1276 ± 4	1291 ± 5	1288 ± 1
Pressure scale height (km)	56 ± 5	61 ± 4	54 ± 3	54.2 ± 0.2	54.2 ± 0.1
Temperature (K)	114 ± 9	108 ± 9	97 ± 5	95 ± 1	95.0 ± 0.1
Source	Millis et al. 1993	Elliot et al. 2003a	Elliot et al. 2007	Person et al. 2008	This work

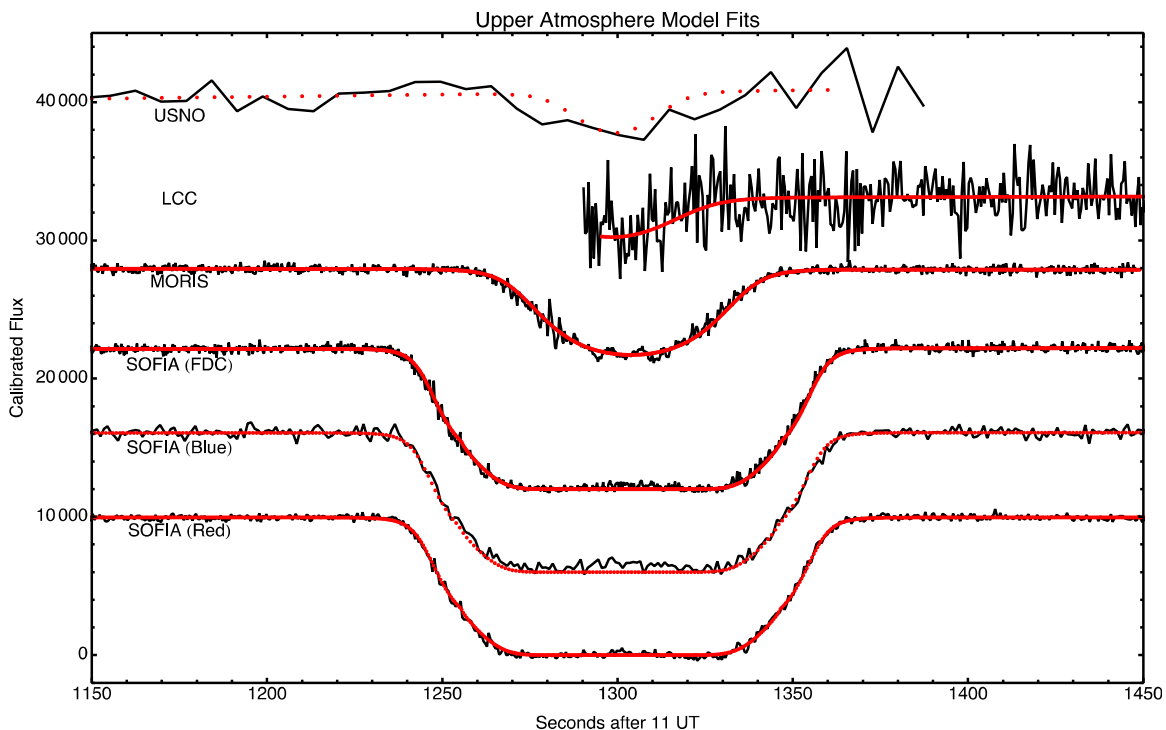


**Figure 9.** Haze model fitted to light curve data. Similarly to Figure 6, this plots the best-fitting model over the data. In this case, the haze model (see text) is used to simulate extinction in the lower atmosphere. Note that now the lower portions of the light curves have an excellent correspondence to the plotted model, unlike in Figure 6 where only the upper portions of the light curves provided acceptable fits. The only significant residuals between the model and the fit occur at the central flash itself, as the haze model depresses the central flash below the observed values.

**Table 6**  
Fitted Haze Parameters from 1988 and 2011

Parameter	1988	2011
Onset radius	1217 km	1244 km
Haze scale-height	29.3 km	22.4 km
Unit optical depth	1205 km	1196 km

As in 1988, adding these three simple model parameters does a remarkable job of describing both the upper and lower portions of the light curves. The best fitting haze model is plotted in Figure 9.

While Figure 9 shows a good correspondence with the data, attempts at haze fitting to the bowl-shaped light curves of 2006 fail completely (Elliot et al. 2007). The resulting haze parameters from this current fit are quite similar to those determined by Millis from the 1988 occultation, with only the onset radius increasing to account for the increase in atmospheric bulk between the two events. A comparison of these parameters is given in Table 6. This similarity would seem to indicate that whatever process is responsible for any haze is fairly consistent, even though the haze signature vanished entirely in the intervening years.

This haze model was supported by a difference in light curve extinction in different wavelengths detected in 2002 (Elliot et al. 2003a), but a similar experiment conducted by Young et al. (2008) failed to reproduce this result indicating that if haze were indeed responsible for the lower atmospheric changes, it is at best intermittent.

Table 7 gives the fitted parameters from all fits, including the upper-atmosphere-only fits and the lower-atmosphere haze modeling. Parameters were allowed to fit to the data where

error bars are given and were fixed otherwise. The “consistent” atmosphere fits indicate that the atmospheric parameters were fixed to the values determined in 2006 (Elliot et al. 2006) to allow direct comparison with previous measurements of the half-light radius.

#### 4.5. Thermal Gradient and Inversion

After the 1988 event, Von Eshleman (1989) and others (Hubbard et al. 1990) proposed a second mechanism that could account for the differences seen in the lower atmosphere, namely a sudden onset thermal gradient much stronger than any seen in the upper atmosphere. Stansberry et al. (1994) further developed this theory in 1994, qualitatively explaining how it could result in the flux decreases seen below the half-light level.

The Elliot and Young light curve model assumes a constant thermal gradient throughout the atmosphere. Attempts to splice together upper and lower atmosphere models with different thermal gradients results in discontinuities at the joint that makes fitting impossible. Light curve inversion does not suffer from this problem and can be applied under certain assumptions, most importantly a lack of extinction. Elliot et al. described this inversion technique together with its assumptions and applied it to the 1988 light curve (Elliot et al. 2003b). Using the upper atmospheric model fits of the previous section as the upper boundary condition for the inversion, we can invert the light curve down from the half-light level and recover the temperature profile, as shown in Figure 10.

The temperature profiles given in Figure 10 are consistent with the 1D atmospheric modeling done by Strobel et al. (1996) if one allows a large (over 3%) concentration of a non- $N_2$  coolant in the atmosphere, such as CO or  $CH_4$ . However, this quantity of

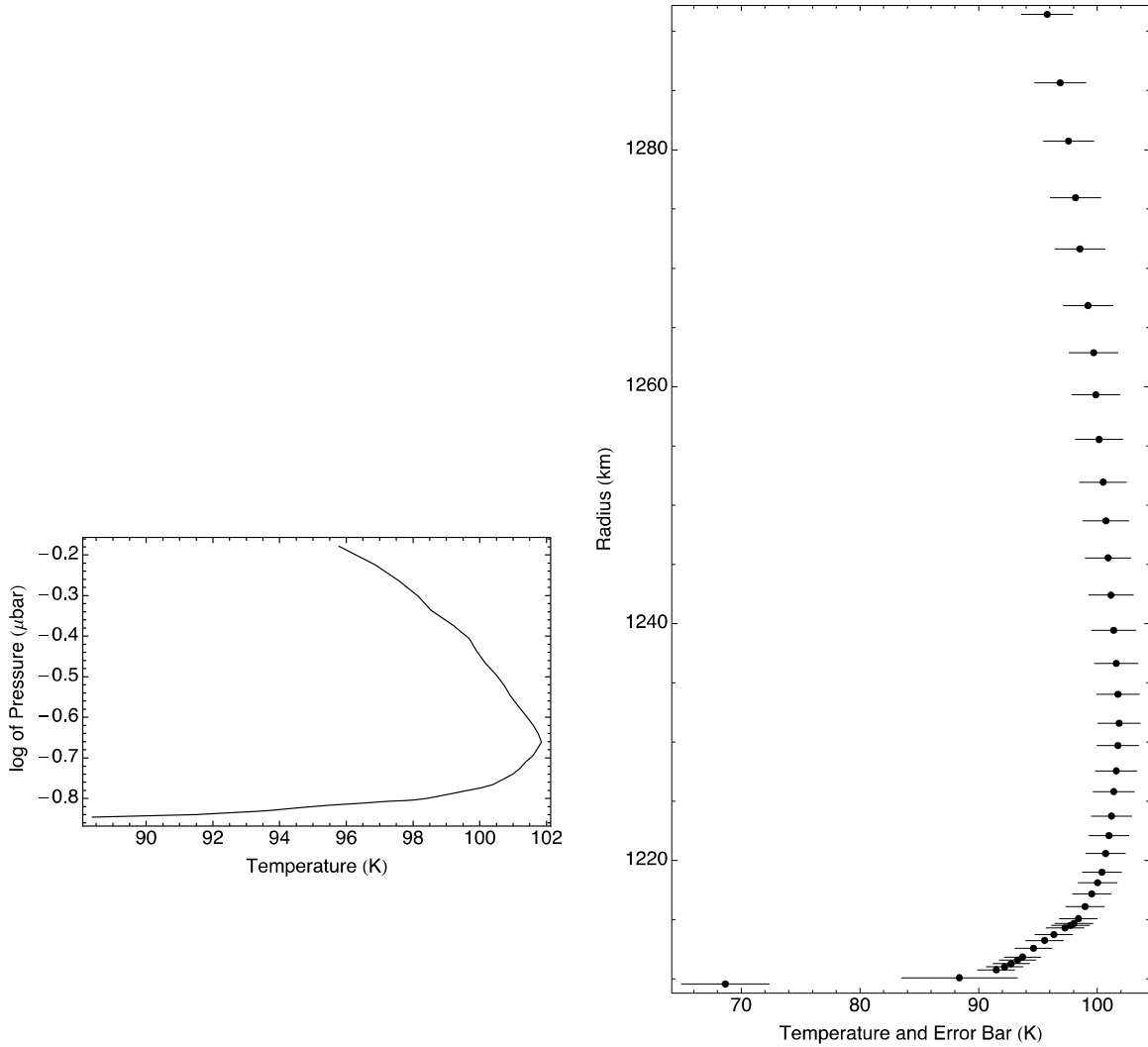


**Figure 10.** Inverted temperature profile derived from the SOFIA (HIPO red) light curve. The temperature profile is plotted against radius (right) and pressure (left) for the emersion portion of this light curve. The immersion inversion results look similar. Note that by approximately one scale height below the half-light level, the temperature gradient reverses from the trend seen in the upper atmosphere, and starts a sharp and rapid decline, getting as low as 70 K before the inversion profile ends.

**Table 7**  
Fitted Parameters from All Atmospheric Fits

Parameter/Fit	Consistent Atmosphere	Free Atmosphere	Haze-consistent Atmosphere	Haze-free Atmosphere
Lower flux cutoff	0.6	0.6	0.0	0.0
Fit-reduced chi-squared	1.11	1.10	1.28	1.25
Half-light radius, $r_h$ (km)	$1290.3 \pm 1.1$	$1288.4 \pm 1.0$	$1291.1 \pm 0.8$	$1289.5 \pm 1.0$
Energy binding ratio, $\lambda_h$	18.3	$14.0 \pm 0.9$	18.3	$18.9 \pm 0.3$
Thermal gradient parameter, $b$	-2.2	$-2.7 \pm 0.4$	-2.2	$0.2 \pm 0.3$
Occultation center, $F_0$	$-3674.0 \pm 1.0$	$-3674.5 \pm 1.1$	$-3673.8 \pm 0.8$	$-3674.4 \pm 0.7$
Occultation center, $G_0$	$4411.5 \pm 2.0$	$4416.8 \pm 2.4$	$4407.7 \pm 1.2$	$4413.6 \pm 1.6$
Haze onset radius (km)	None	None	$1243.9 \pm 1.6$	$1245.3 \pm 2.2$
Haze scale-height (km)	None	None	$22.4 \pm 0.9$	$18.7 \pm 1.0$
Haze unit optical depth (km)	None	None	$1196.0 \pm 0.5$	$1197.8 \pm 1.2$

coolant exceeds the 0.5% surface values established by infrared spectroscopic observations (Young et al. 1997; Owen et al. 1993).

#### 4.6. Central Flash Fitting

The final feature of the light curves to be analyzed is the weak central flash seen in all three SOFIA light curves. The brightening is also distinctly off-center. As we have seen,

the upper atmospheric fits produce a central flash that is grossly too bright at the close approach of SOFIA to the center of the shadow (104 km) and attempting to fit the upper and lower atmospheres separately results in unacceptable discontinuities. We therefore focus on the haze and thermal inversion models to examine the brightness of the central flash.

In principle, the best approach for modeling the central flash based on the inversion is to use the inverted atmospheric

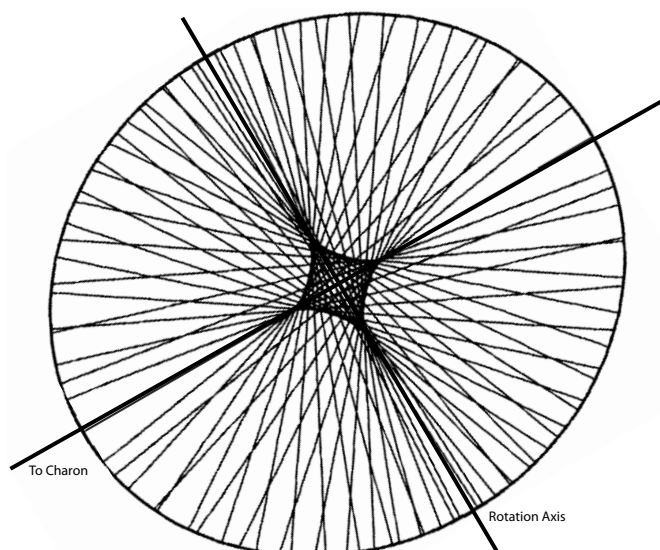


**Figure 11.** Sample evolute model: this model has a 6% ellipticity exaggerated by a factor of three for clarity. Note that each light ray is refracted along the perpendicular to the limb, but with an elliptical figure, the limb angle is constantly changing. The diamond-shaped figure (the evolute) in the middle shows how the central flash is spread out from a single central point by the uneven refraction.

temperature and pressure profiles to construct a fully physical model of the atmosphere and propagate light through this model to reconstruct model light curves (Chamberlain & Elliot 1997). This very time- and computation-intensive procedure is unwarranted for the tiny central flash seen, as the small size of the flash does not provide sufficient leverage on the various atmospheric parameters in the physical model.

Instead, we fit a simple evolute model based upon an elliptical (cross-section) atmosphere with only two parameters, the apparent ellipticity of the atmosphere, and the orientation of the major axis of this ellipse to search for the best-fitting parameters that result in the appropriate amount of offset from the central peak, and the apparently single-peaked signature

of the evolute. A sample evolute model, with exaggerated ellipticity for clarity, is shown in Figure 11.

Figure 12 shows the results of the best-fitting case of this model. In order to get the general flux levels low enough to allow for fitting the overall shape, we used a strong (perhaps unphysical) thermal gradient of  $20 \text{ K km}^{-1}$ . This thermal gradient does not at all fit the top of the light curve (as expected), but depresses the flux levels in the lower portions enough that the ellipticity can be fit against the offset of the central flash from the occultation mid-time. Holding the major axis of the ellipse fixed in the direction toward Charon, we measure a fitted ellipticity of  $0.06 \pm 0.01$ . This fitted ellipticity is a lower limit to the actual atmospheric ellipticity due to projection of the full ellipticity into the sky-plane observed by the occultation. This fitted ellipticity is similar to those determined by occultation chord geometries in the 1988 ( $0.091 \pm 0.041$ ) and 2002 ( $0.066 \pm 0.040$ ) events (Person 2006), although these geometric ellipticities should be lower than the deeper values resulting from central flash measurements, due to the central flash probing much more deeply into Pluto’s gravity well. Unfortunately, given that most of our data in this event occur at the same location, we are unable to derive a geometric ellipticity for the present epoch to compare to the central flash ellipticity.

The haze model fails to reproduce the central flash at any size when given enough haze to fit the rest of the light curve. This is also shown in Figure 12.

## 5. DISCUSSION

### 5.1. Evolution of Pluto’s Atmosphere

On first inspection it seems that the general character of Pluto’s light curves has changed once again. In 1988, the light curve exhibited a sharp “knee” which slowly faded out over the next couple of decades, becoming shallow in 2002, and almost completely bowl-shaped by 2006. Now, in 2011, the knee seems to have returned, indicating that whatever clarifying process has been occurring in the atmosphere has now reversed. For the extinction explanation, this could imply some sort of cyclic or intermittent haze production, by some form of cryo-volcanism or burst-driven pollutant production during rapid

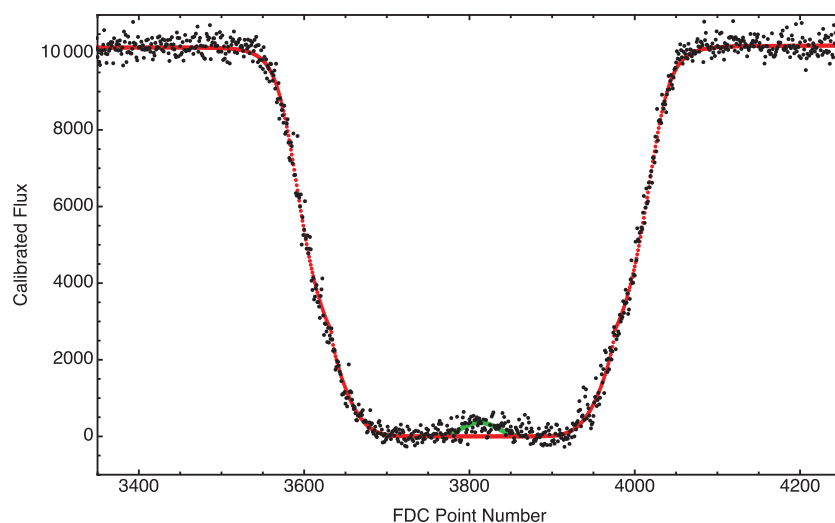


**Figure 12.** Central flash fit. Here, the FDC light curve is plotted in black, with the best-fitting lower atmospheric haze model overplotted in red. In the bottom 10% of the light curve this is overplotted in green by the simple evolute model with a strong thermal gradient (see text). The thermal gradient model follows the flux increase in the central portion of the light curve reasonably well, while the haze model is almost flat throughout this region. This best-fitting evolute has a fitted ellipticity of  $0.06 \pm 0.01$  for isobars in Pluto’s atmosphere in the region probed (approximately 1200 km radius).

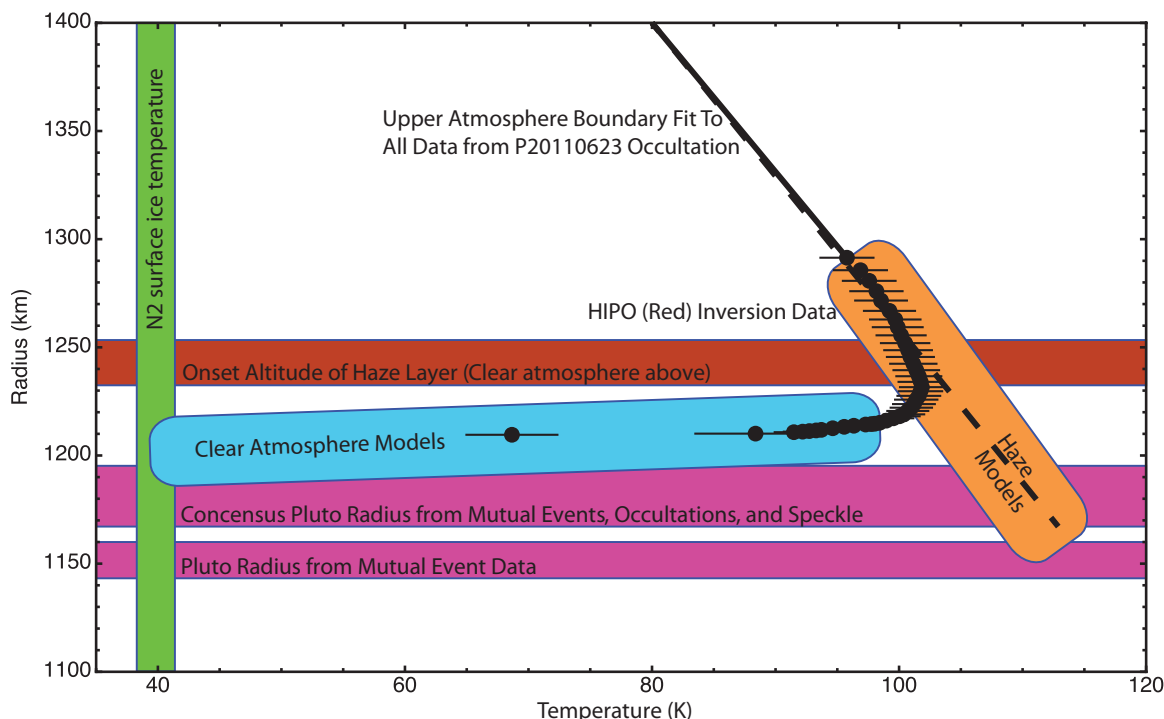


**Figure 13.** Pluto atmosphere model summary. The best-fitting upper atmospheric model (Elliot & Young 1992) is plotted with the solid black line. The dotted extension with error bars is the inversion results (Elliot et al. 2003b) using the solid line model as a boundary condition and assuming a hazeless atmosphere. The particulate haze extinction assumption extends this model down the dashed line, as represented by the orange box (although it must also eventually return to the surface temperature). The blue box shows the temperature models for the clear atmosphere assumption. The correct model should eventually reach both a reasonable value for the surface radius of the planet (Young 1994; Person et al. 2006) and the surface ice temperature (Tryka et al. 1994; Lellouch et al. 2009). Note that the clear atmosphere models favor larger radii, and the haze models favor smaller radii.

surface ice sublimation. One of the main difficulties with these haze explanations is that particulate settling times on Pluto should be fairly short. Even taking generous values for diffusion coefficients, and taking particle sizes much smaller than the  $1 \mu\text{m}$  particles postulated from multi-wavelength analyses (Thomas-Osip et al. 2002) so that diffusive processes dominate, one would still expect haze settling times on the order of just a year. So a slow diffusive settling of haze that is replenished over the course of decades (from 1988 to 2011) seems difficult to reconcile.

Generating a deep troposphere that slowly thins over the course of two decades and then suddenly reasserts itself is also difficult in a timeframe only 9% of a Pluto year. Haze transport models that predict the rapid rise in Pluto’s atmospheric pressure during the first part of that era fail to have a symmetric feature in the latter part of the era to reassert the lost troposphere (Hansen & Paige 1996). Rather, they prefer this period to be a small part of a multi-decadal oscillation on the order of Pluto’s seasons.

Figure 13 shows the two competing explanations plotted against radius from Pluto’s surface extrapolating from the known inversion data given above down to the surface region. One possible discriminating parameter would be a hard measure of the actual surface radius. At the moment, estimates of the surface radius from occultation model fitting still result in error bars of almost half an atmospheric scale height (Person et al. 2006) although recent efforts at combining numerical radiative-transfer atmospheric models with occultation light curve fitting are giving hope for reducing this uncertainty (Zalucha et al. 2011a). To date, however, the most advanced models (Zalucha et al. 2011b) still require enough assumptions about the state of Pluto’s atmosphere so as to render the surface radii speculative.

## 5.2. Pluto’s Atmospheric Structure

As seen in Figure 12, the observed central flash was offset from the occultation mid-time, indicating that the SOFIA aircraft skirted one corner of the evolute (see Figure 11). Thermal gradient models require a very steep gradient to reproduce the flux levels of the central flash and occultation baseline, but fail to fit the upper atmospheric portions of the light curve. The haze model fits the lower atmospheric portions of the light curve easily, but eliminates the central flash. Thus the presence of the weak central flash seems to argue for a combination of these two solutions (the orange and blue areas of Figure 13) resulting in a moderate haze with a swift onset, coupled with a deep troposphere. Given that the characteristic variable extinction of a haze solution was seen in the past, though not in the current event, the changing nature of the lower atmosphere (Figure 8) seems to indicate either a stable lower troposphere with varying amounts of light haze, or a very dynamic lower atmosphere with significant variations in decadal timescales.

In the upper atmosphere, evidence of the wave structure detected in 2007 (Person et al. 2008; Hubbard et al. 2009; McCarthy et al. 2008) is seen in the upper portion of the light curve inversion of the SOFIA curves (see Figure 10), but is much more apparent in the structure of the MORIS light curve (Figure 5). As a high-altitude graze, the central portion of the MORIS light curve samples the upper atmosphere much more strongly than the deeper SOFIA light curves, which have a much lower vertical sample rate in the upper atmosphere due to their almost perpendicular approach to the limb. The MORIS light curve is very symmetric about its center point in the lowest portion of the curve, but this symmetry appears to break down

as you move up the curve, possibly indicating that the wave structure is less coherent at the upper-most radii. This was not the case in the 2007 event, where the light curves were symmetric across their entire extent, indicating that the wave structures were coherent across much of the planet (Person et al. 2007). This may indicate that the wave phenomena seen in 2007 are weaker in 2011, perhaps having to do with the change in steepness in the thermal gradient now seen in the lower atmosphere, although the light curves obtained in 2007 have almost four times the S/N of the 2011 MORIS curve.

The fitted ellipticity ( $0.06 \pm 0.01$ ) of the atmosphere is consistent with previous measurements of Pluto's atmospheric asphericity (Person 2006; Olkin et al. 2007). Supporting this level of ellipticity requires significant surface winds ( $\sim 200 \text{ m s}^{-1}$ ) or high-altitude winds approaching the sonic velocity. This sort of superrotation has been postulated in the past (Del Genio & Zhou 1996; Person 2006), although at lesser strengths than those needed to support these winds. Interestingly, this superrotation state requires a strong troposphere with temperature decreasing rapidly near the surface (Del Genio & Zhou 1996).

Such winds were recently simulated in a 2D general circulation model for Pluto that exhibited high-speed, high-latitude jets encircling the poles (Zalucha & Gulbis 2012). As the current modeling does not include mass transport due to the expected frost cycle, a fuller solution involving a 3D general circulation model is in development by A. Zalucha (2013, private communication). These measurements of permissible overall atmospheric ellipticity should provide significant constraints on such models.

## 6. CONCLUSIONS AND FURTHER WORK

The first airborne observations of a Pluto stellar occultation since 1988 were a significant success. The combined light curves from the various observations of the event indicate a stable atmosphere, slightly contracted since the 2007 measurements, but still in the generally stable temperature and pressure configuration that has persisted since 2006.

The mysterious “knee” in the light curve, indicative of a sudden onset of a troposphere or haze layer has returned, after slowly fading away over the decades since the last airborne observations. Likely caused by a combination of both particulate extinction and thermal inversion, this feature's disappearance and reappearance seems to indicate some cyclic or intermittent process unaccounted for in current frost migration or global circulation models.

The central flash, which was not observable without SOFIA's mobility and last-minute redeployment options, indicates an elliptical atmosphere characterized by high global winds, or more likely lesser zonal winds producing Pluto's atmospheric oblateness.

Still to come are complete analyses of the color differences between the various SOFIA channels as contrasted with color differences from the full spectral data obtained at the IRTF. Also, detailed analysis of the Pluto–Charon separation is possible and will be forthcoming due to the nearly central chord afforded by SOFIA, precisely fixing Pluto's location when combined with ground sources.

All in all, we see once again that Pluto has an extremely complex and dynamic atmosphere, with both spatial and temporal variations, which should provide an extremely rich data opportunity for the *New Horizons* spacecraft in 2015. However, even with the expected fantastic returns from that mission, the time-variability of the atmosphere, and the small size of fea-

tures such as the central flash, require continued monitoring from both fixed telescopes and mobile platforms such as the SOFIA aircraft.

The authors would like to acknowledge the late Prof. James Elliot of MIT, whose vision and unswerving persistence carried many of us through the era between the final KAO observations and these first SOFIA observations of Pluto.

We also acknowledge Adam Kraus for providing Keck data to check for duplicity of the occultation star during the prediction process, and Georgi Mandushev for assisting with the analysis of similar duplicity data obtained at the Magellan telescopes.

This work was supported in part by NASA Planetary Astronomy grants NNX10AB27G to MIT, NNX08AO50G and NNX11ZDA001N to Williams College, and USRA grant #8500-98-003 to Lowell Observatory.

This research is based in part on observations made with the NASA/DLR Stratospheric Observatory for Infrared Astronomy (SOFIA). SOFIA is jointly operated by the Universities Space Research Association, Inc. (USRA) under NASA contract NAS2-97001 and the Deutsches SOFIA Institut (DSI) under DLR contract 50 OK 0901 to the University of Stuttgart.

A.A.S.G. acknowledges funding from the National Research Foundation of South Africa. A.A.S.G. and J.P.E. were visiting astronomers at the Infrared Telescope Facility, which is operated by the University of Hawaii under Cooperative Agreement no. NNX-08AE38A with the National Aeronautics and Space Administration, Science Mission Directorate, Planetary Astronomy Program. D.A. was a Keck Northeast Astronomy Consortium Summer Fellow, supported by the Research Experiences for Undergraduates program of the National Science Foundation under grant AST-1005024.

## REFERENCES

- Alard, C. 2000, *A&AS*, **144**, 363  
 Chamberlain, D. M., & Elliot, J. L. 1997, *PASP*, **109**, 1170  
 Del Genio, A. D., & Zhou, W. 1996, *Icar*, **120**, 332  
 Dunham, E. W., Elliot, J. L., Bida, T. A., & Taylor, B. W. 2004, *Proc. SPIE*, **5492**, 592  
 Dunham, E. W., Elliot, J. L., Bida, T. A., et al. 2008, *Proc. SPIE*, **7014**, 70144Z  
 Elliot, J. L., Ates, A., Babcock, B. A., et al. 2003a, *Natur*, **424**, 165  
 Elliot, J. L., Dunham, E. W., Bosh, A. S., et al. 1989, *Icar*, **77**, 148  
 Elliot, J. L., Dunham, E. W., & Mink, D. 1977a, *Natur*, **267**, 328  
 Elliot, J. L., French, R. G., Dunham, E., et al. 1977b, *ApJ*, **217**, 661  
 Elliot, J. L., & Olkin, C. B. 1996, in *Annual Review of Earth and Planetary Sciences, Probing Planetary Atmospheres with Stellar Occultations*, ed. G. W. Wetherill, A. L. Albee, & K. C. Burke (Palo Alto, CA: Annual Reviews Inc.), 89  
 Elliot, J. L., Person, M. J., Gulbis, A. A. S., et al. 2006, *BAAS*, **38**, 541  
 Elliot, J. L., Person, M. J., Gulbis, A. A. S., et al. 2007, *AJ*, **134**, 1  
 Elliot, J. L., Person, M. J., & Qu, S. 2003b, *AJ*, **126**, 1041  
 Elliot, J. L., & Young, L. A. 1992, *AJ*, **103**, 991  
 Eshleman, V. R. 1989, *Icar*, **80**, 439  
 Gulbis, A. A. S., Bus, S. J., Elliot, J. L., et al. 2011, *PASP*, **123**, 461  
 Gulbis, A. A. S., Elliot, J. L., Person, M. J., et al. 2006, *BAAS*, **38**, 541  
 Hansen, C. J., & Paige, D. A. 1996, *Icar*, **120**, 247  
 Hubbard, W. B., McCarthy, D. W., Kulesa, C. A., et al. 2009, *Icar*, **204**, 284  
 Hubbard, W. B., Yelle, R. V., & Lunine, J. I. 1990, *Icar*, **84**, 1  
 Lellouch, E., Sicardy, B., de Bergh, C., et al. 2009, *A&A*, **495**, L17  
 McCarthy, D., Kulesa, C., Hubbard, W., et al. 2008, *AJ*, **136**, 1519  
 Millis, R. L., Wasserman, L. H., Franz, O. G., et al. 1993, *Icar*, **105**, 282  
 Olkin, C. B., Elliot, J. L., Hammel, H. B., et al. 1997, *Icar*, **129**, 178  
 Olkin, C. B., Young, E. F., Young, L., et al. 2007, *BAAS*, **39**, 520  
 Owen, T. C., Roush, T. L., Cruikshank, D. P., et al. 1993, *Sci*, **261**, 745  
 Pasachoff, J. M., Souza, S. P., Babcock, B. A., et al. 2005, *AJ*, **129**, 1718  
 Person, M. J. 2006, PhD thesis, Massachusetts Institute of Technology  
 Person, M. J., Elliot, J. L., Bosh, A. S., et al. 2010, *BAAS*, **42**, 983  
 Person, M. J., Elliot, J. L., Gulbis, A. A. S., et al. 2006, *AJ*, **132**, 1575  
 Person, M. J., Elliot, J. L., Gulbis, A. A. S., et al. 2007, *BAAS*, **39**, 519

- Person, M. J., Elliot, J. L., Gulbis, A. A. S., et al. 2008, *AJ*, **136**, 1510
- Rayner, J. T., Toomey, D. W., Onaka, P. M., et al. 2003, *PASP*, **115**, 362
- Sallum, S. 2012, S. B. thesis, Massachusetts Institute of Technology
- Sicardy, B., Boissel, Y., Colas, F., et al. 2009, Constraints on Charon's Orbit from the Stellar Occultation of 22 June 2008, European Planetary Science Congress 2009, <http://meetings.copernicus.org/epsc2009>, p. 164
- Sicardy, B., Widemann, T., Lellouch, E., et al. 2003, *Natur*, **424**, 168
- Stansberry, J. A., Lunine, J. I., Hubbard, W. B., Yelle, R. V., & Hunten, D. M. 1994, *Icar*, **111**, 503
- Strobel, D. F., Zhu, X., Summers, M. E., & Stevens, M. H. 1996, *Icar*, **120**, 266
- Thomas-Osip, J. E., Elliot, J. L., & Clancy, K. B. 2002, *BAAS*, **34**, 1212
- Tody, D. 1986, *Proc. SPIE*, **627**, 733
- Tryka, K. M., Brown, R. H., Cruikshank, D. P., et al. 1994, *Icar*, **112**, 513
- Wolfram, S. 1991, *Mathematica* (Redwood City, CA: Addison-Wesley)
- Young, E. F., French, R. G., Young, L. A., et al. 2008, *AJ*, **136**, 1757
- Young, L. A. 1994, PhD thesis, Massachusetts Institute of Technology
- Young, L. A., Elliot, J. L., Tokunaga, A., et al. 1997, *Icar*, **127**, 258
- Young, L. A., Howell, R. R., French, R. G., et al. 2011, Occultations by Pluto and Charon Observed by the PHOT Team, EPSC-DPS Joint Meeting 2011, <http://meetings.copernicus.org/epsc-dps2011>, p. 1341
- Zacharias, N., Urban, S. E., Zacharias, M. I., et al. 2004, *AJ*, **127**, 3043
- Zalucha, A., & Gulbis, A. A. S. 2012, *JGR*, **117**, 14
- Zalucha, A., Gulbis, A. A. S., Zhu, X., Strobel, D. F., & Elliot, J. L. 2011a, *Icar*, **211**, 804
- Zalucha, A., Zhu, X., Gulbis, A. A. S., Strobel, D. F., & Elliot, J. L. 2011b, *Icar*, **214**, 685